UNIVERSITY
OF TRENTO

DEPARTMENT OF INFORMATION AND COMMUNICATION TECHNOLOGY

38050 Povo – Trento (Italy), Via Sommarive 14
http://www.dit.unitn.it

IMPROVED MICROWAVE IMAGING PROCEDURE FOR NON-DESTRUCTIVE EVALUATIONS OF TWO-DIMENSIONAL STRUCTURES

Salvatore Caorsi, Andrea Massa, Matteo Pastorino,
and Massimo Donelli

June 2003

Technical Report # DIT-03-040

Also: presented at IMTC2003, special session on Imaging Systems; submitted for consideration for publication, special issue IMTC2003 of the IEEE Transactions on Instrumentation and Measurement

Improved Microwave Imaging Procedure for Non-Destructive Evaluations of Two-Dimensional Structures

Salvatore Caorsi*, *Member*, *IEEE*, Andrea Massa**, *Member*, *IEEE*, Matteo Pastorino***, *Senior Member*, *IEEE*, and Massimo Donelli**

* Department of Electronics,

University of Pavia, Via Ferrata 1, 27100 Pavia - Italy

Tel. +39 0382 505661, Fax +39 0382 422583, E-mail: *caorsi@ele.unipv.it*

** Department of Information and Communication Technology,

University of Trento, Via Sommarive 14, 38050 Trento - Italy

Tel. +39 0461 882057, Fax +39 0461 882093, E-mail: *andrea.massa@ing.unitn.it*

*** Department of Biophysical and Electronic Engineering,

University of Genoa, Via Opera Pia 11/A, 16145 Genoa - Italy

Tel. +39 010 3532796, Fax +39 010 3532245, E-mail: *pastorino@dibe.unige.it*

Improved Microwave Imaging Procedure for Non-Destructive Evaluations of Two-Dimensional Structures

Salvatore Caorsi*, *Member*, *IEEE*, Andrea Massa**, *Member*, *IEEE*, Matteo Pastorino***, *Senior Member*, *IEEE*, and Massimo Donelli**

Key words: Nondestructive Evaluation, Microwave Imaging, Genetic Algorithms, Green's Function.

Abstract

An improved microwave procedure for detecting defects in dielectric structures is proposed. The procedure is based on the integral equations of the inverse scattering problem. A hybrid Genetic Algorithm is applied in order to minimize the obtained nonlinear functional. Since in nondestructive evaluations the unperturbed object is completely known, it is possible off-line to numerically compute the Green's function for the configuration without defects. Consequently, a very significant computation saving is obtained, since the "*chromosome*" of the Genetic Algorithm codes only the parameters describing the unknown defect.

1 Introduction

Nondestructive evaluation (NDE) and nondestructive testing (NDT) are fields in which microwaves can play a further increasing role, although this frequency range has been already recognized to be very important for practical diagnostic applications [1]-[5]. Further possibilities are offered by combining the diagnostic capabilities of microwaves with the imaging potentialities of inverse scattering techniques [6]-[9]. At present, electromagnetic imaging methods, based on inversion procedures, are already widely used in NDE/NDT applications, mainly with reference to eddy-current approaches [10]. On the contrary, further work is needed to make microwave-based inverse system to be effective, mainly due to difficulties related to the inverse scattering problem at microwave frequencies [11]. Such a problem is nonlinear, ill-posed and local solutions may correspond to wrong diagnoses, in most cases really unacceptable. Recently, iterative procedures have been devised, which, starting from measured scattered data, are able to define the scattering configuration corresponding to the global minimum. Stochastic minimization approaches are now rather common in electromagnetics [12]-[15]. The genetic algorithm (GA) is one of the widest used minimization tools of this kind [16]-[18]. The main limitations of stochastic optimization approaches concern the rate of convergence toward the right solution, due to the random nature of the operation involved. Consequently, they are strongly dependent on an efficient parameterization of the problem. In other words, it is mandatory to limit the search space of the approach and, contemporarily, to reduce the number of problem unknowns. This goal can be accomplished only if the approach is able to efficiently include the available a priori information into the model. A preliminary version of this approach, called "Free-space Green's function Approach" (FGA), was proposed in [19]. In that paper, the defect to be detected was approximately described by few parameters to be determined during the minimization process, which was based on free-space scattering concepts. However, the main limitations of that approach was the need for

considering the internal total electric field as a further problem unknown. Consequently, the unknown array contained a parameterization of the distribution of the total electric field inside the whole cross section. Moreover, the field distribution changes for different illumination conditions. Then, if a multi-illumination multiview approach is used, the field distribution must be kept as an unknown for each illumination/view. As a result, the "chromosomes" coding the trial solutions of the GA are extremely long and mainly contain unnecessary information. In the present paper, a different approach is considered. In NDE/NDT applications the unperturbed geometry is *a-priori* known. This is a key point which distinguish this problem to other imaging applications. The known unperturbed configuration can be taken into account in the forward scattering formulation. In particular, the inverse problem can be reformulated only involving integral equations extended to the geometric domain of the defect (estimated at each iteration). The kernel of the integral equations is the Green's function [20] for the unperturbed geometry, which can be computed, analytically or numerically, off-line and once for all. Then, the problem unknowns are reduced to the parameterization of the defect and to the electric field inside the defect only. The result is a sharp reduction in the "chromosome" dimension and, consequently, in the computational time, as will be shown in Sections IV and V, where several dielectric configurations containing defects are simulated and reconstructed.

2 Mathematical Formulation

Let us consider the cylindrical geometry shown in Fig. $1(a)$. S is a fixed area on a plane orthogonal to the cylinder axis (i.e., parallel to the z axis) occupied by an host medium characterized by known dielectric properties (dielectric permittivity, $\varepsilon_I(x,y)$, and electric conductivity, $\sigma_I(x,y)$) and embedded in a homogeneous external medium, $(\varepsilon_0, \sigma_0)$. S includes, at an unknown position (x_C, y_C), the cross section D of a cylindrical homogeneous crack whose shape and material characteristics, $(\varepsilon_C, \sigma_C)$, are unknown. This

scenario is successively illuminated by a number of known TM-polarized incident fields, $\overline{E}^{v}_{inc}(\overline{\rho}) = E^{v}_{inc}(x,y)\,\widehat{z}$, $v = 1, ..., V$, being $\overline{\rho} = x\widehat{x} + y\widehat{y}$. The working frequency is f_0. According to these notations, the electric field $E^{v}_{tot}(x,y)$, corresponding to the incident field $E^{v}_{inc}(x,y)$, can be expressed as follows [21]:

$$E^{v}_{tot}(x,y) = E^{v}_{inc}(x,y) + \int\int_{S} \tau_S(x',y')\, E^{v}_{tot}(x',y')\, G_0(k_0 r)\, dx'dy' \tag{1}$$

where G_0 is the two-dimensional free-space Green's function [20] and

$$\tau_S(x,y) = \begin{cases} \varepsilon_I(x,y) - 1 - j\frac{\sigma_I(x,y)}{2\pi f_0 \varepsilon_0} & if \;\; (x,y) \in S_D \equiv S - D \\ \varepsilon_C - 1 - j\frac{\sigma_C}{2\pi f_0 \varepsilon_0} & if \;\; (x,y) \in D \end{cases} \tag{2}$$

.

On the other hand, it is possible to rewrite (1) in a more convenient form:

$$\begin{aligned} E^{v}_{tot}(x,y) = E^{v}_{inc}(x,y) + \int\int_{S} \tau_{S_D}(x',y')\, E^{v}_{tot(cf)}(x',y')\, G_0(x,y/x',y')\, dx'dy' \\ + \int\int_{D} \widetilde{\tau}_D(x',y')\, E^{v}_{tot}(x',y')\, G_I(x,y/x',y')\, dx'dy' \end{aligned} \tag{3}$$

where $\tau_{S_D}(x,y)$ is the unperturbed object function given by $\tau_{S_D}(x,y) = \varepsilon_I(x,y) - 1 - j\frac{\sigma_I(x,y)}{2\pi f_0 \varepsilon_0}$ $(x,y) \in S$, $\widetilde{\tau}_D(x,y)$ is a "differential" object function such that $\widetilde{\tau}_D(x,y) = \tau_S(x,y) - \tau_{S_D}(x,y)$, and $E^{v}_{tot(cf)}$ is the electric field related to the incident field, $E^{v}_{inc}(x,y)$, for the crack-free scenario. G_I is the Green's function for the unperturbed structure, which satisfies the following integral equation

$$G_I(x,y/x',y') = G_0(x,y/x',y') + \int\int_{S} \tau_{S_D}(x'',y'')\, G_I(x'',y''/x',y')\, G_0(x,y/x'',y'')\, dx''dy'' \tag{4}$$

Since the sum of the first two terms at the right-hand side of the equation (3) can be seen as the "incident" field on the crack, once G_I has been computed, the scattering problem is limited to the "differential object" occupying the defect area D.

Numerically, equation (4) can be solved by using the Richmond's theory [22]. If the region S is partitioned in N square sub-domains, (4) assumes the following algebraic form

$$G_{nt}^{I} = G_{nt}^{0} + \sum_{m=1\,(m\neq k)}^{N} \tau_{m}^{S_D} G_{mt}^{I} \int\int_{A_m} G_0\left(x_n, y_n / x'', y''\right) dx''dy'' \quad n,k = 1,...,N \tag{5}$$

with $n = 1,...,N$, $t = k + \Lambda_{kn}$, $k = 1,...,N-1$, being $\Lambda_{ij} = 0$ if $i < j$ or $\Lambda_{ij} = 1$ if $i \geq j$. In Eq. (5), $G_{nt}^{I} = G_I\left(x_n, y_n / x_t, y_t\right)$, $G_{nt}^{0} = G_0\left(x_n, y_n / x_t, y_t\right)$, and $\tau_{m}^{S_D} = \tau_{S_D}\left(x_m, y_m\right)$ being (x_j, y_j) the center of the j-th subdomain of area A_j. The computation of G_{nt}^{I} requires the solution of N systems of equations given by

$$[G_n]\,\underline{g}_n = \underline{g_0}_n \quad n = 1,...,N \tag{6}$$

where $\underline{g}_n$ and $\underline{g_0}_n$ are $(N-1)\times 1$ arrays whose elements are given by $\left\{\underline{g}_n\right\}_t = G_{nt}^{I}$ and $\left\{\underline{g_0}_n\right\}_t = G_{nt}^{0}$, respectively. Moreover, the $(N-1)\times(N-1)$ elements of the square matrix $[G_n]$ are given by $\{[G_n]\}_{mk} = \delta_{mk} - \tau_t^{S_D} \int\int_{A_t} G_0\left(x_u, y_u / x'', y''\right) dx''dy''$ where $u = m + \Lambda_{km}$, $m = 1,...,N-1$.

Fortunately, as shown in [23], if $[G]$ is a $N \times N$ matrix from which $[G_n]$ is obtained by deleting the n-th row and the n-th column, the matrix $[G_n]^{-1}$ can be easily determined by neglecting the same row and column of the matrix $[F]\,[G]^{-1}$ where $[F]$ is a rather empty matrix whose non-vanishing elements are directly obtained from the elements of $[G]$ as follows

$$\{[F]\}_{mk} = \begin{cases} 0 & if \quad m \neq k \quad and \quad k \neq j \\ 1 & if \quad m = k \quad and \quad k \neq j \\ -\frac{\{[G]\}_{mk}}{\{[G]\}_{kk}} & if \quad m \neq k \quad and \quad k = j \\ \frac{1}{\{[G]\}_{kk}} & if \quad m = k \quad and \quad k = j \end{cases} \qquad m,k,j = 1,...,N \tag{7}$$

In order to detect the presence of an homogeneous crack in the original scatterer, the

crack is approximated by an object of rectangular shape and parameterized by length, ℓ, width, w, orientation, θ, and center coordinates, (x_C, y_C) to be determined during the reconstruction process. Under this hypothesis, the object function describing the defect results

$$\widetilde{\tau}_D(x,y) = \begin{cases} \tau_S - \tau_{S_D}(x,y) & X \in \left[-\frac{\ell}{2}, \frac{\ell}{2}\right] \; and \; Y \in \left[-\frac{w}{2}, \frac{w}{2}\right] \\ 0 & otherwise \end{cases} \tag{8}$$

where $X = (x - x_C)\, cos\theta + (y - y_C)\, sin\theta$, $Y = (x_C - x)\, sin\theta + (y - y_C)\, cos\theta$. Moreover, the internal electric field for the flaw configuration is unknown. Consequently, the reconstruction process is aimed at searching for the unknown array $\Psi = \{x_C,\, y_C,\, \ell,\, w,\, \theta;\, E^v_{tot}(x,y)\ (x,y) \in D\}$ minimizing the following cost function:

$$\Phi\{\Psi\} =$$

$$\frac{\alpha}{V}\sum_{v=1}^{V}\left\{\frac{\int\int_{S_{obs}}\left|\left[E^v_{scatt}(x,y) - E^v_{scatt(cf)}(x,y)\right] - \int\int_D \widetilde{\tau}_D(x',y')\, E^v_{tot}(x',y')\, G_I(x,y/x',y')\, dx'dy'\right|^2 dxdy}{\int\int_{S_{obs}}\left|E^v_{scatt(cf)}(x,y)\right|^2 dxdy}\right\}$$

$$\frac{\beta}{V}\sum_{v=1}^{V}\left\{\frac{\int\int_D\left|E^v_{tot(cf)}(x,y) - E^v_{tot}(x,y) + \int\int_D \widetilde{\tau}_D(x',y')\, E^v_{tot}(x',y')\, G_I(x,y/x',y')\, dx'dy'\right|^2 dxdy}{\int\int_D\left|E^v_{inc}(x,y)\right|^2 dxdy}\right\} \tag{9}$$

where $E^v_{scatt(cf)}(x,y) = \int\int_S \tau_{S_D}(x',y')\, E^v_{tot(cf)}(x',y')\, G_0(x,y/x',y')\, dx'dy'$ (being $E^v_{scatt(cf)}(x,y) = E^v_{tot(cf)}(x,y) - E^v_{inc}(x,y)$) and $E^v_{tot(cf)}$ are known quantities. After discretization [22], Equation (9) assumes the following expression:

$$\Phi\{\psi\} =$$

$$\frac{\alpha}{MV}\sum_{v=1}^{V}\sum_{m=1}^{M}\left\{\frac{\left|\left[E^v_{scatt}(x_m,y_m) - E^v_{scatt(cf)}(x_m,y_m)\right] - \sum_{n=1}^{N}\widetilde{\tau}_D(x_n,y_n)\, E^v_{tot}(x_n,y_n)\, A_n G^I_{mn}\right|^2}{\left|E^v_{scatt}(x_m,y_m)\right|^2}\right\} +$$

$$\frac{\beta}{NV}\sum_{v=1}^{V}\sum_{n=1}^{N}\left\{\frac{\left|E^v_{tot(cf)}(x_n,y_n) - E^v_{tot}(x_n,y_n) + \sum_{p=1}^{N}\widetilde{\tau}_D(x_p,y_p)\, E^v_{tot}(x_p,y_p)\, A_p G^I_{np}\right|^2}{\left|E^v_{inc}(x_n,y_n)\right|^2}\right\} \tag{10}$$

where α and β are two regularizing constants, $\psi = \{x_C, y_C, \ell, w, \theta; E^v_{tot}(x_p, y_p), p = 1, ..., P\}$, $(x_p, y_p) \in D \subset S$ denotes the center of the p-th discretization domain belonging to the crack area (P being the number of discretization domains of the crack) (Fig. $1(b)$), and (x_m, y_m) indicates the m-th measurement point ($(x_m, y_m) \in S_{obs}$, $m = 1, ..., M$). According to the adopted discretization, it is convenient to assume that ℓ, w, θ are discrete variables $\ell = j\Delta$, $j = 1, ..., L$, $w = i\Delta$, $i = 1, ..., W$, $\theta = u\Delta\theta$, $u = 1, ..., U$, being $\Delta = \sqrt{A_n}$ and $\Delta\theta$ the angular step used for the multiview process.

In order to minimize (10), a suitable GA [16] is used to define a sequence of trial configurations, $\psi^{(h)}, h = 1, ..., H$, ($h$ being the iteration number) which converges to an extremum of the functional.

3 Description of the GA-based Optimization Procedure

GAs [16][17] are efficient optimization techniques that mimics the genetic adaptation occurring in natural evolution. The algorithm processes a population of candidate solutions, $\overline{\psi}^{(h)} = \left\{\psi^{(h)}_q, q = 1, ..., Q\right\}$ being Q the population dimension. The quality of the solutions of the current population is evaluated according to the scalar cost function, $\Phi^{(h)}_q = \Phi\left\{\psi^{(h)}_q\right\}$. The individuals that achieve higher fitness values (corresponding to lower values of the cost function) are more likely to be selected as *parents* and generate new solutions (called *offspring*) by means of *crossover* and *mutation*. Generally, crossover promotes the exchange of genetic information among elements of the population. The offspring are subject to mutations, which randomly modify the genetic structures of trial solutions in order to create new variants. The current population is replaced by the newly generated group of offspring, $\overline{\psi}^{(h)} \Leftarrow \overline{\psi}^{(h+1)}$. The evolutionary procedure terminates either if a maximum number of generations elapses ($h = H$) or a fixed value of the cost function is reached ($\Phi^{(h^*)}_{opt} = min_q\left\{\Phi^{(h^*)}_q\right\} \leq \eta$, η being the convergence threshold and $h = h^*$ the iteration of convergence).

In order to deal with NDE/NDT problems, it is necessary to customize the GA by defining a suitable encoding procedure and, accordingly, genetic operators. In this respect, too, the new procedure (named "Inhomogeneous Green's function Approach" - IGA) is very different from the one proposed in [19]. In particular, hybrid-coded variable-length chromosomes are used, in which each trial solution, $\psi_{IGA} = \{x_C, y_C, \ell, w, \theta; E^v_{tot}(x_p, y_p), p = 1, ..., P\}$, $(x_p, y_p) \in D \subset S$, is coded by using the concatenated multi-parameter scheme (Fig. $2(a)$). The use of a variable-length chromosome is necessary due to the variable dimension (i.e., different crack area in correspondence with different trial solutions) of the domain where the unknown field is computed. On the contrary, the FGA approach considers hybrid-coded fixed length chromosomes (being $\psi_{IGA} = \{x_C, y_C, \ell, w, \theta; E^v_{tot}(x_p, y_p), p = 1, ..., P\}$, $(x_p, y_p) \in S$ the corresponding trial solution) due to the fixed dimension of the area where $E^v_{tot}(x_p, y_p)$ is computed (i.e., the host medium area, S).

As far as the genetic operators are concerned, the mutation operators are defined according to [19] and the crossover is modified in order to allow variable-length chromosomes. In more detail, Fig. $2(b)$ describes the crossover operation when the cross-position lies into the binary part of the chromosome and the defect of the produced offspring occupies a number of sub-domains equal to or smaller than that occupied by one of their parent ($P^{(h+1)}_{q_a} \leq max_b \left\{P^{(h)}_{q_b}\right\}$, $a, b = 1, 2$), being

$$\begin{aligned} \left\{E^v_{tot}(x_p, y_p)\right\}^{(h+1)}_{q_1} &= \frac{r\left\{E^v_{tot}(x_p,y_p)\right\}^{(h)}_{q_1} + (1-r)\left\{E^v_{tot}(x_p,y_p)\right\}^{(h)}_{q_2}}{2}, \quad p = 1, ..., P^{(h+1)}_{q_1} \\ \left\{E^v_{tot}(x_p, y_p)\right\}^{(h+1)}_{q_2} &= \frac{(1-r)\left\{E^v_{tot}(x_p,y_p)\right\}^{(h)}_{q_1} + r\left\{E^v_{tot}(x_p,y_p)\right\}^{(h)}_{q_2}}{2}, \quad p = 1, ..., P^{(h+1)}_{q_2} \end{aligned} \tag{11}$$

$P^{(h)}_q = i^{(h)}_q \times j^{(h)}_q$ and $r \in [0, 1]$ is a random number. On the other hand (Fig. $2(c)$), if $P^{(h+1)}_{q_a} > max_b \left\{P^{(h)}_{q_b}\right\}$, $a, b = 1, 2$, then

$$\left\{E^v_{tot}(x_p, y_p)\right\}^{(h+1)}_{q_a} = E^v_{tot(cf)}(x_p, y_p), \; p = \left(max_b \left\{P^{(h)}_{q_b}\right\} + 1\right), ..., P^{(h+1)}_{q_a} \quad a, b = 1, 2 \tag{12}$$

Moreover, Fig. $2(d)$ illustrates the crossover when the cross-position lies into the real part of the chromosome. Let us assume that $P_{q_a}^{(h)} > P_{q_b}^{(h)}$, $a \neq b$ and let be $p = p_c$ the crossover position. Then, the real-part of the chromosome results as follows

$$\begin{aligned}
\left\{E_{tot}^{v}\left(x_p, y_p\right)\right\}_{q_b}^{(h+1)} &= \begin{cases} \left\{E_{tot}^{v}\left(x_p, y_p\right)\right\}_{q_b}^{(h)} & p = 1, ..., p_c \\ \left\{E_{tot}^{v}\left(x_p, y_p\right)\right\}_{q_a}^{(h)} & p = \left(p_c + 1\right), ..., P_{q_b}^{(h)} \end{cases} \\
\left\{E_{tot}^{v}\left(x_p, y_p\right)\right\}_{q_a}^{(h+1)} &= \begin{cases} \left\{E_{tot}^{v}\left(x_p, y_p\right)\right\}_{q_a}^{(h)} & p = 1, ..., p_c \\ \left\{E_{tot}^{v}\left(x_p, y_p\right)\right\}_{q_b}^{(h)} & p = \left(p_c + 1\right), ..., P_{q_b}^{(h)} \\ E_{tot(cf)}^{v}\left(x_p, y_p\right) & p = \left(P_{q_b}^{(h)} + 1\right), ..., P_{q_a}^{(h)} \end{cases}
\end{aligned} \tag{13}$$

4 Numerical Results

In this section, selected numerical results are shown in order to assess the effectiveness of the proposed approach. For illustrating the dependence of the reconstruction quality on the most critical experimental and numerical parameters, an exhaustive numerical analysis has been performed, which is deeply analyzed in the following. Toward this end, the following experimental parameters and error figures are defined:

- Signal-to-noise ratio (SNR):

$$SNR = 10log_{10}\frac{\sum_{v=1}^{V}\sum_{m=1}^{M}\left|E_{scatt}^{v}\left(x_m, y_m\right)\right|^2}{2MV\sigma_{noise}^2} \tag{14}$$

  where σ_{noise}^2 is the variance of the additive Gaussian noise (with zero mean value).

- Error on the location of the center of the crack, δ_C:

$$\delta_C = 10log_{10}\left\{\frac{\sqrt{\left(x_C - \widehat{x}_C\right)^2 + \left(y_C - \widehat{y}_C\right)^2}}{d_{max}} \times 100\right\} \tag{15}$$

  being $(\widehat{x}_C, \widehat{y}_C)$ the estimated coordinates of the crack, and d_{max} the maximum error in defining the crack center when it belongs to the host scatterer.

- Error on the estimation of the crack area:

$$\delta_A = 10log_{10}\left\{\left|\frac{A_C - \widehat{A}_C}{A_C}\right| \times 100\right\} \tag{16}$$

where $\widehat{A}_C$ and A_C are the estimated and actual crack areas, respectively.

- Index of the convergence rate:

$$\Delta_{conv} = \frac{h^*_{FGA} - h^*_{IGA}}{H} \tag{17}$$

where h^*_{IGA} and h^*_{FGA} are the number of iterations required to attain the convergence threshold with the FGA and the IGA, respectively.

As far as the reference scenario is concerned, let us consider a square homogeneous cylinder $l = \frac{4}{5}\lambda$ in side characterized by an object function $\tau_{S_D} = 1$ and probed by $V = 4$ plane-wave incident fields given by $E^v_{inc}(x,y) = e^{-jk_0(xcos\phi^v + ysin\phi^v)}$ being $\phi^v = (v-1)\frac{2\pi}{V}$, $v = 1, ..., V$. The values of the scattered electric field have been collected at $M = 81$ equally spaced measurement points located on a circular observation domain ($r = \frac{32}{15}\lambda$ being the radius). In order to simulate noisy data for assessing the sensitivity of the method to the noise, a white Gaussian noise has been added to noiseless data (numerically computed by solving the direct problem) with decreasing values of the SNR from $30\,dB$ to $2.5\,dB$.

According to the guidelines suggested in [14][18], the following parameters of the GA have been assumed: $Q = 80$, $P_c = 0.7$ (crossover probability), $P_m = 0.12$ (mutation probability), and $P_{bm} = 0.01$ ("bit" mutation probability), $H = 600$, and $\eta = 10^{-5}$.

4.1 Impact of the Crack Dimensions on the Reconstruction

The first computational test is aimed at evaluating the reconstruction accuracy for different dimensions of the crack. Toward this end, a void crack ($\tau_D = 0.0$) is centered at point $x_C = y_C = \frac{\lambda}{10}$. The area of the flaw changes from $A_C = 25 \times 10^{-4}\lambda^2$ to $A_C = 25 \times 10^{-2}\lambda^2$. Such a configuration has been earlier treated in [19]. In Figure 3, a color-level representation of the error figures related to the crack reconstruction of the IGA and FGA methods are shown. As far as the crack location is concerned (Figs. $3(a)$ and $3(b)$), the performances of the IGA method turn out to be similar to that achieved with the FGA approach as confirmed from the average values of the localization error ($av\{\delta_C\}_{IGA} = 7.55\,dB$ and $av\{\delta_C\}_{FGA} = 8.0\,dB$). However, the proposed method considerably overcomes our previous technique [19] in estimating the crack area ($av\{\delta_A\}_{IGA} = 12.0\,dB$ versus $av\{\delta_A\}_{FGA} = 17.0\,dB$).

4.2 Impact of the Crack Position on the Reconstruction

Another test of the IGA concerns the reconstruction capabilities of the approach for different positions of the defect inside the host medium. In this example, the crack (being $A_C = 25.6 \times 10^{-3}\lambda^2$) is moved along the diagonal of the host medium from the center to a distance equal to $d = 0.49\lambda$. Figure 4 shows the reached results in term of error figures. As for the FGA method (Fig. $4(b)$ and $4(d)$), the errors in the reconstruction do not depend on the crack position. For the IGA, too, the impact of the location of the crack inside the host medium can be reasonably neglected and the resolution of the algorithm is strongly related to the signal-to-noise ratio. However, starting from $SNR = 15\,dB$, the IGA procedure guarantees a significant improvement resulting in a localization error lower than $6\,dB$ (being $av\{\delta_C\}_{IGA} = 13.6\,dB$) and $\{\delta_A\}_{IGA} \leq 10\,dB$.

4.3 Impact of the Host-medium Conductivity on the Reconstruction

The final example concerns a more complex scenario in which the defect lies into a lossy host medium with constant complex contrast. The crack, 0.2λ-sided, is centered at the point $x_C = y_C = 0.1\lambda$ inside an host medium whose conductivity is varied from $\sigma_I = 0.1\,\frac{S}{m}$ to $\sigma_I = 1.0\,\frac{S}{m}$. The improvement of the quality of the reconstructions by using the new method is clearly pointed out in Figure 5 where the error figures yielded by the two methods are shown. The enhancement in the reconstruction accuracy is evident for both the location (Figs. $5(a)$-$5(b)$) and the estimation of area of the crack (Figs. $5(c)$-$5(d)$). In more detail, the capabilities of the proposed approach can be highlighted by observing that $12\,dB \geq \{\delta_C\}_{IGA} \geq -50\,dB$ ($24\,dB \geq \{\delta_C\}_{IGA} \geq 12\,dB$) and $av\,\{\delta_A\}_{IGA} = 12.24\,dB$ ($av\,\{\delta_A\}_{FGA} = 18.22\,dB$).

5 Computational Issues

A key point in developing an inverse scattering technique for NDE is the computational load. Generally speaking, the main drawback of numerical methods based on evolutionary codes lies in the large computational time. Such a time should be strongly decreased in order to considerably reduce the overall turnaround time for diagnostic work. In this framework, the IGA method significantly improves the results achieved with the FGA approach [19] not only in term of the resolution of the imaging procedure but also from the point of view of the computational effectiveness. The computational effort required by the IGA approach is substantially lower, so that a reliable solution can be achieved in about $\frac{1}{8}$ of the time necessary for the FGA. Such a result has been achieved with a strong reduction of the time needed to complete each iteration and by increasing the convergence rate of the procedure. Table I gives an idea of the computational saving allowed by the

IGA. It results that each iteration took on an average approximately 1.35 *sec* and 3.36 *sec* for the IGA and FGA methods on a PC computer (Intel Celeron Mobile 600 MHz - 64 Mb RAM), respectively.

Moreover, the reduction of the search space with the use of the Green's function for the unperturbed configuration yielded an increase of the convergence rate of the optimization procedure. In order to highlight this key point, the average number of iterations required to achieve a solution is reported in Table II. As expected, it can be observed that the ratio $\xi^* = \frac{av\{h^*_{FGA}\}}{av\{h^*_{IGA}\}}$ results greater than 2.5 ranging from 2.71 to 3.37. For completeness, Figure 6 shows the index of the convergence rate for all the test previously described.

6 Conclusions and Future Developments

An improved inversion technique for electromagnetic evaluation and testing has been proposed. The approach combines the capabilities of a customized hybrid-coded genetic algorithm in finding the global minimum of a functional with the effectiveness of the use of the Green's function for the unperturbed configuration. The results of several numerical simulations have been presented in order to evaluate the location accuracy of void cracks even in presence of significant noise levels in the input data as well as in dissipative host media. The new approach allows a significant computational saving by including, in an efficient way, the *a-priori* knowledge available on the unperturbed configuration.

As far as the future developments of the proposed method are concerned, the arising reduction of the overall computational burden (in term of memory saving and increasing of the convergence rate) seems to indicate a possible extension from the two-dimensional case to the three-dimensional situation making 3D NDE/NDT problems "reachable" by means of electromagnetic-based techniques. However, it will be possible to furtherly investigate this possibility when suitable test-cases (or complete benchmarks) will be available and a further improvement of the measurement techniques (and experimental apparatus) will

be achieved in order to prevent measurement errors and to reduce the effects of the measurement noise.

Acknowledgement

The authors wish to thank Dr. F. Righini and Ing. A. Rosani for helpful discussions on genetic algorithms and for providing numerical results of computer simulations.

References

[1] R. Zoughi. *Microwave Nondestructive Testing and Evaluation*, Kluwer Academic Publishers, The Netherlands, 2000.

[2] M. Tabib-Azar, "Applications of an ultra high resolution evanescent microwave imaging probe in the nondestructive testing of materials," *Materials Evaluation*, vol. 59, pp. 70-78, 2001.

[3] S. J. Lockwood and H. Lee, "Pulse-echo microwave imaging for NDE of civil structures: Image reconstruction, enhancement, and object recognition," *Int. J. Imaging Systems Technol.*, vol. 8, pp. 407-412, 1997.

[4] R. J. King and P. Stiles, "Microwave nondestructive evaluation of composites," *Review of Progress in Quantitative Nondestructive Evaluation*, vol. 3, pp.1073-81, Plenum, New York, 1984.

[5] K. Meyer, K. J. Langenberg, and R. Schneider, "Microwave imaging of defects in solids," *Proc. 21st Annual Review of Progress in Quantitative NDE*, Snowmass Village, Colorado, USA, July 31 - Aug. 5, 1994.

[6] W. C. Chew and Y. M. Wang, "Reconstruction of two-dimensional permittivity distribution using the distorted Born iterative method," *IEEE Trans. on Medical Imaging*, vol. 9, pp. 218-225, 1990.

[7] C. C. Chiu and P. T. Liu, "Image reconstruction of a perfectly conducting cylinder by the genetic algorithm," *IEE Proc. Microw. Antennas Propag.*, vol. 3, p. 143, 1996.

[8] K. Belkebir, Ch. Pichot, J. Ch. Bolomey, P. Berthaud, G. Gottard, X. Derobert and G. Fauchoux, "Microwave tomography system for reinforced concrete structures," *Proc. 24th European Microwave Conf.*, Cannes, France, pp. 1209-1214, 1994.

[9] S. Caorsi, A. Massa, and M. Pastorino, "A computational technique based on a real-coded genetic algorithm for microwave imaging purposes," *IEEE Trans. Geosci. Remote Sensing*, Special Issue on "Computational Wave Issues in Remote Sensing, Imaging and Target Identification, Propagation, and Inverse Scattering," vol. 38, n. 4, part I, pp. 1697-1708, 2000.

[10] V. Bertrand, D. Lesselier, and S. Mastorchio, "Numerical modeling of eddy current non-destructive evaluation with FEM-BEM Trifou software in controlled configurations," in: S. S. Udpa et al., eds., *Electromagnetic Nondestructive Evaluation IV*, pp. 32-41, IOS Press, Amsterdam 2000.

[11] M. Bertero and P. Boccacci. *Introduction to Inverse Problems in Imaging*, IOP, Bristol, UK, 1998.

[12] R. L. Haupt, "An introduction to genetic algorithms for electromagnetics," *IEEE Antennas Propagat. Magazine*, vol. 37, pp. 7-15, 1995.

[13] D. S. Weile and E. Michielssen, "Genetic algorithm optimization applied to electromagnetics: a review," *IEEE Trans. Antennas Propagat.*, vol. 45, pp. 343-353, March 1997.

[14] J. M. Johnson and Y. Rahmat-Samii, "Genetic algorithms in engineering electromagnetics," *IEEE Trans. Antennas Propagat. Magaz.*, vol. 39, no.4, pp. 7-25, 1997.

[15] Y. Rahmat-Samii and E. Michielssen. *Electromagnetic Optimization by Genetic Algorithms*, John Wiley & Sons Inc., New York, 1999.

[16] D. E. Goldberg, *Genetic Algorithms in Search, Optimization, and Machine Learning*, Addison-Wesley, Reading, Mass., 1989.

[17] J. H. Holland. *Adaptation in Natural and Artificial Systems*, Ann Arbor, MI: Univ. Michigan Press, 1975.

[18] R. L. Haupt and S. E. Haupt. *Practical Genetic Algorithms*, John Wiley & Sons Inc., New York, 1998.

[19] S. Caorsi, A. Massa, and M. Pastorino, "A crack identification microwave procedure based on a Genetic Algorithm for non-destructive testing," *IEEE Trans. Antennas Propagat.*, vol. 49, n. 12, pp. 1812-1820, 2001.

[20] C. T. Tai. *Dyadic Green's Functions in Electromagnetic Theory*, International Textbooks, Scranton, 1971.

[21] A. Ishimaru. *Electromagnetic Wave, Propagation, Radiation and Scattering.* Prentice-Hall, 1991.

[22] J. H. Richmond, "Scattering by a dielectric cylinder of arbitrary cross-section shape," *IEEE Trans. Antennas Propagat.*, vol. 13, pp. 334-341, 1965.

[23] S. Caorsi, G. L. Gragnani, M. Pastorino, and M. Rebagliati, "A model-driven approach to microwave diagnostics in biomedical applications," *IEEE Trans. Microwave Theory Tech.*, vol. 44, pp. 1910-1920, 1996.

FIGURE CAPTIONS

- Figure 1.

  Problem Geometry. (a) Two-dimensional scenario and (b) cell numbering.

- Figure 2.

  Example of (a) a hybrid-coded variable-length chromosome ($P = i \times j$). Single-point crossover when the crossover point belongs to the binary part of the chromosome and (b) $P_{q_a}^{(h+1)} \leq max_b \left\{ P_{q_b}^{(h)} \right\}$, $a, b = 1, .2$ or (c) $P_{q_1}^{(h+1)} > max_b \left\{ P_{q_b}^{(h)} \right\}$, $b = 1, 2$. Single-point crossover when the crossover point belongs to the real part of the chromosome (d).

- Figure 3.

  Reconstruction errors for different areas of the crack and for different values of the signal-to-noise ratio. $(a)(b)$ δ_C, and $(c)(d)$ δ_A. $(a)(c)$ IGA and $(b)(d)$ FGA procedures.

- Figure 4.

  Reconstruction errors for different positions of the crack and for different values of the signal-to-noise ratio. $(a)(b)$ δ_C, and $(c)(d)$ δ_A. $(a)(c)$ IGA and $(b)(d)$ FGA procedures.

- Figure 5.

  Reconstruction errors for different values of the electric conductivity of the host medium and for different values of the signal-to-noise ratio. $(a)(b)$ δ_C, and $(c)(d)$ δ_A. $(a)(c)$ IGA and $(b)(d)$ FGA procedures.

- Figure 6.

  Convergence rate estimation: (a) $\Delta_{conv} = \Delta_{conv}(A_C, SNR)$, (b) $\Delta_{conv} = \Delta_{conv}\left(\frac{d}{\lambda}, SNR\right)$, (c) $\Delta_{conv} = \Delta_{conv}(\sigma_I, SNR)$.

TABLE CAPTIONS

- Table I.

  Times required for each iteration of the minimization procedure.

- Table II.

  Number of iterations necessary to achieve the convergence of the iterative procedure.

  (a) Test case 1, (b) Test case 2, (c) Test case 3.

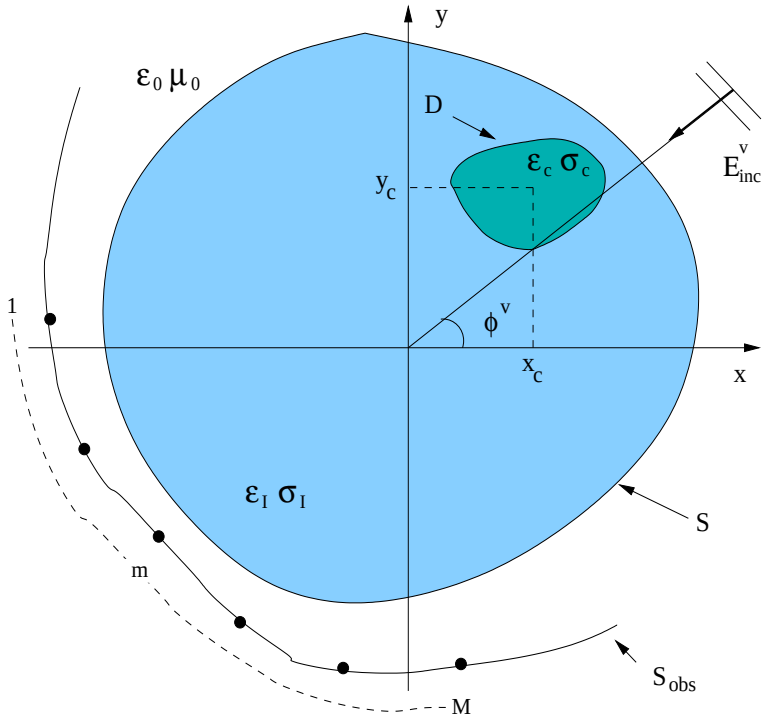

(*a*)

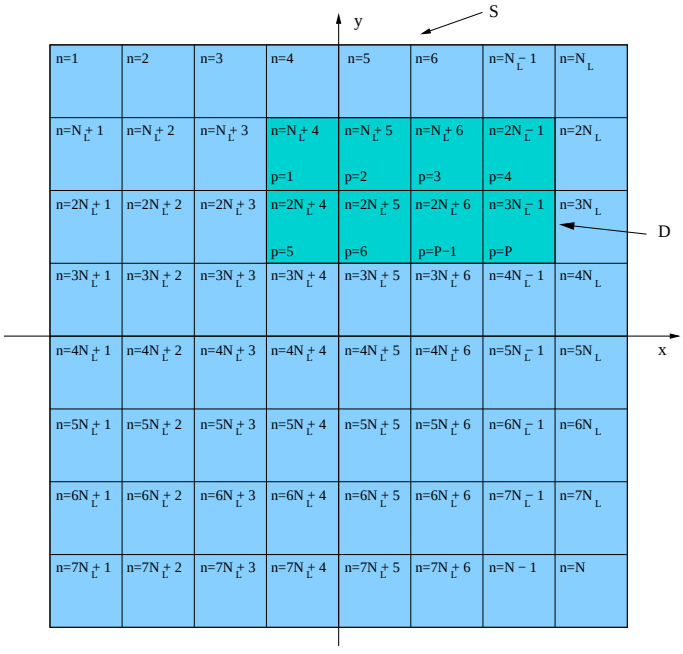

(*b*)

Fig. 1 - S. Caorsi et *al.*, "Improved Microwave Imaging Procedure ..."

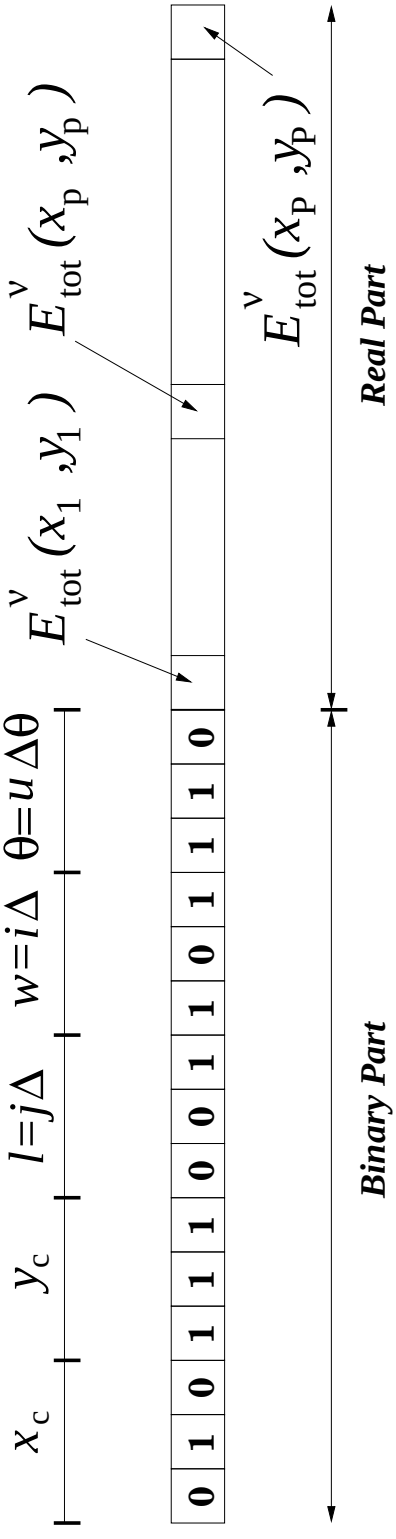

(*a*)

Fig. 2(*I*) - S. Caorsi et *al.*, "A Crack Identification Microwave Procedure ..."

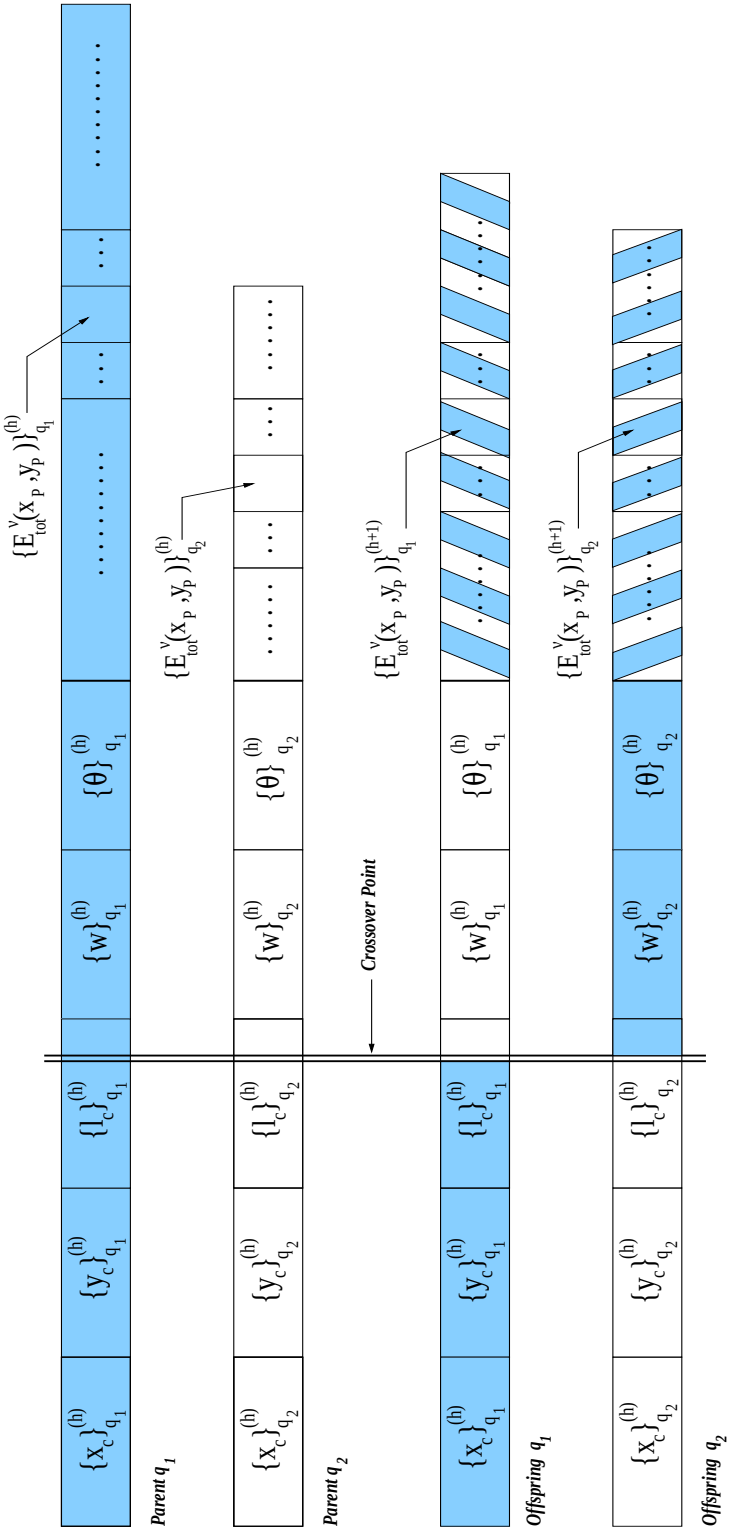

(*b*)

Fig. 2(*II*) - S. Caorsi et *al.*, "A Crack Identification Microwave Procedure ..."

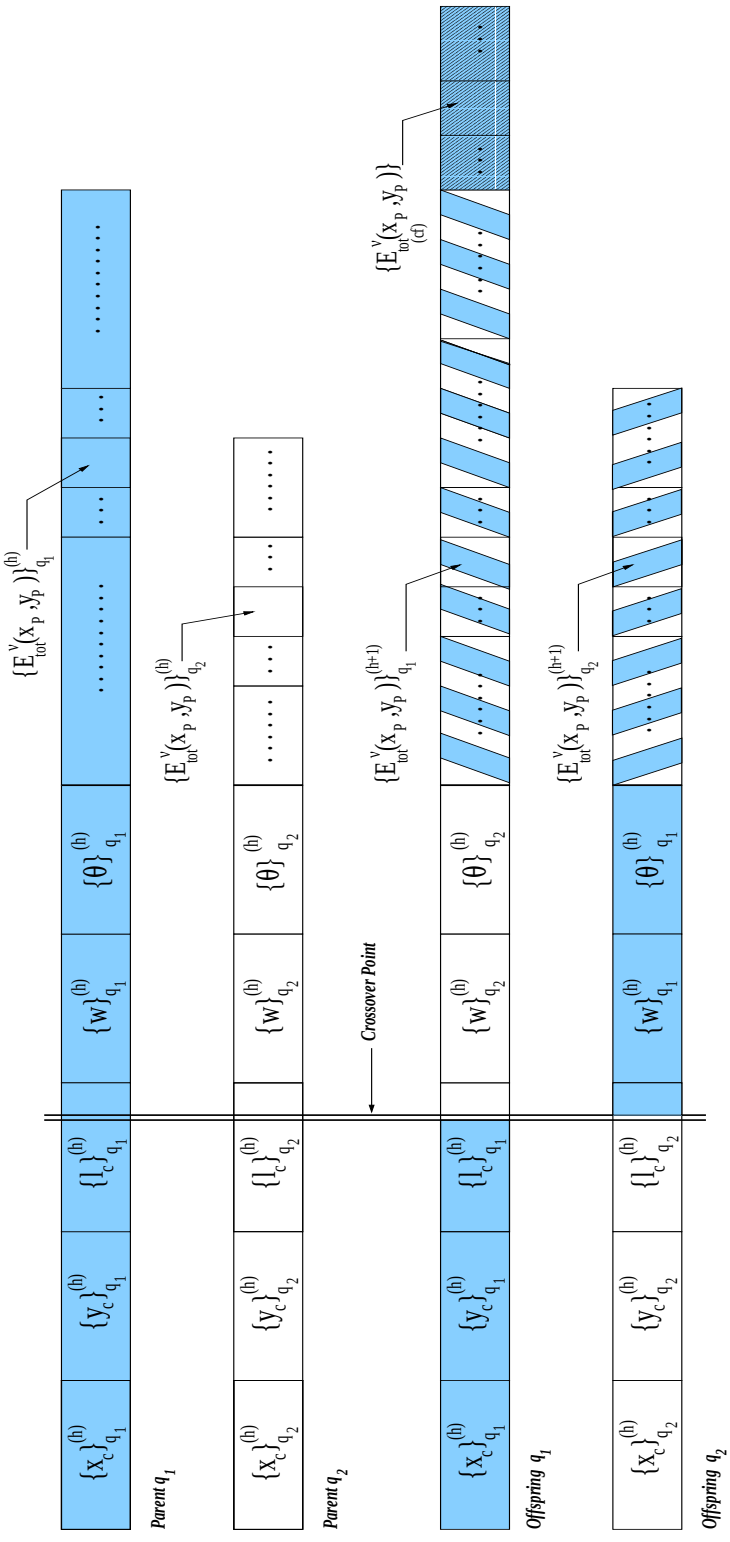

(*c*)

Fig. 2(*III*) - S. Caorsi et *al.*, "A Crack Identification Microwave Procedure ..."

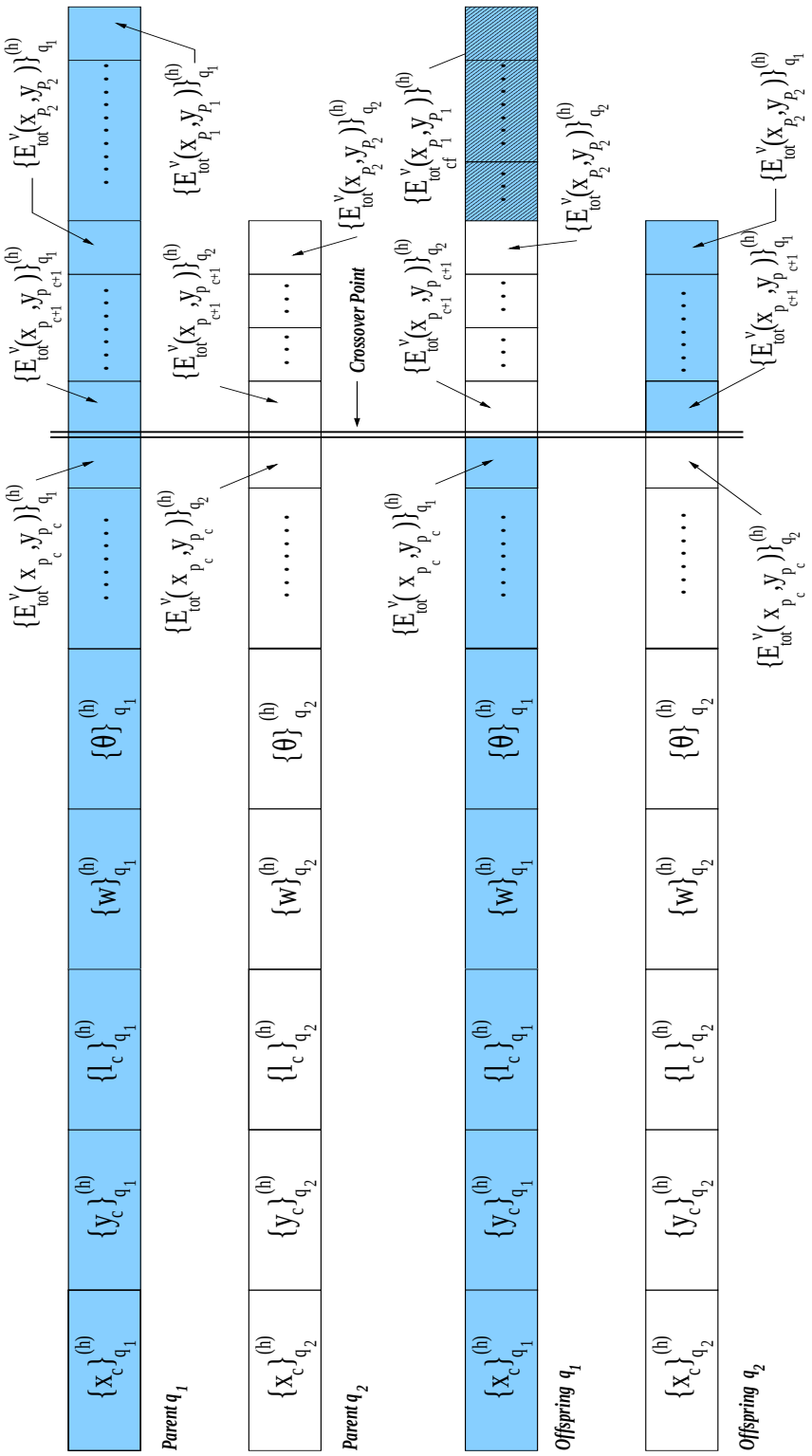

(d)

Fig. 2(IV) - S. Caorsi et *al.*, "A Crack Identification Microwave Procedure ..."

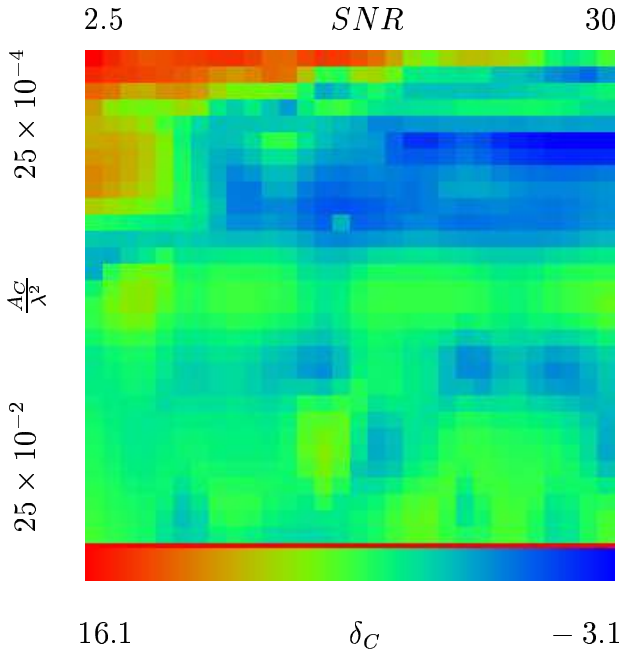

(a)

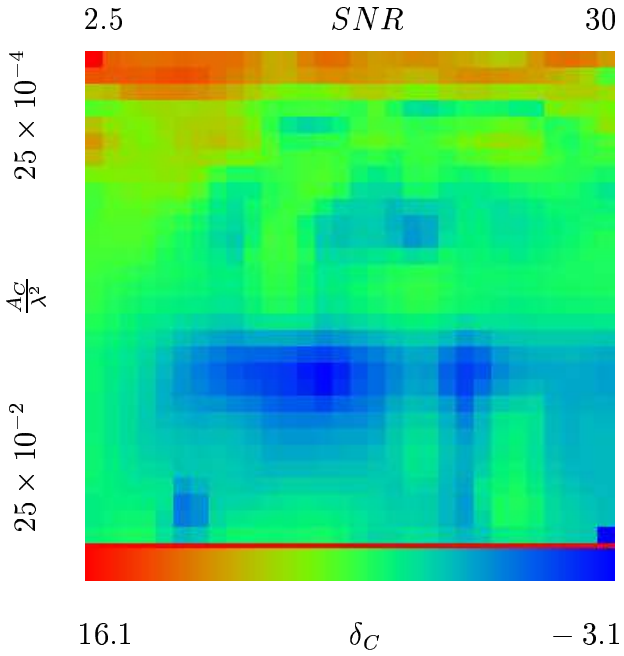

(b)

Fig. 3(I) - S. Caorsi et *al.*, "Improved Microwave Imaging Procedure ..."

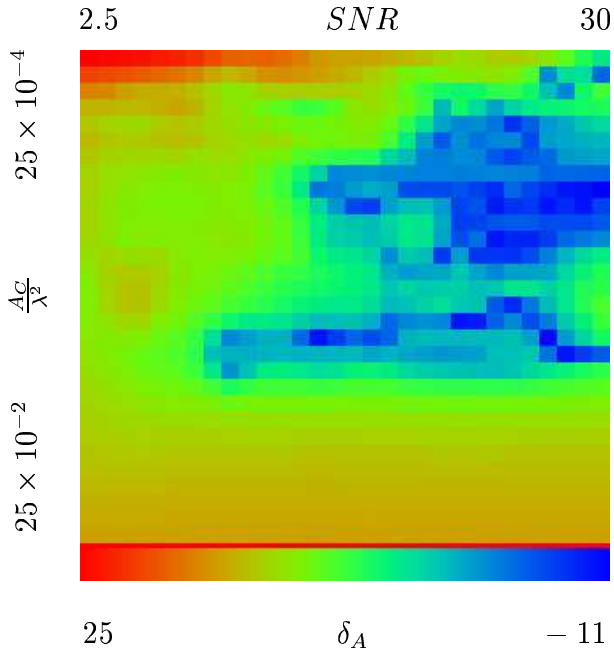

(c)

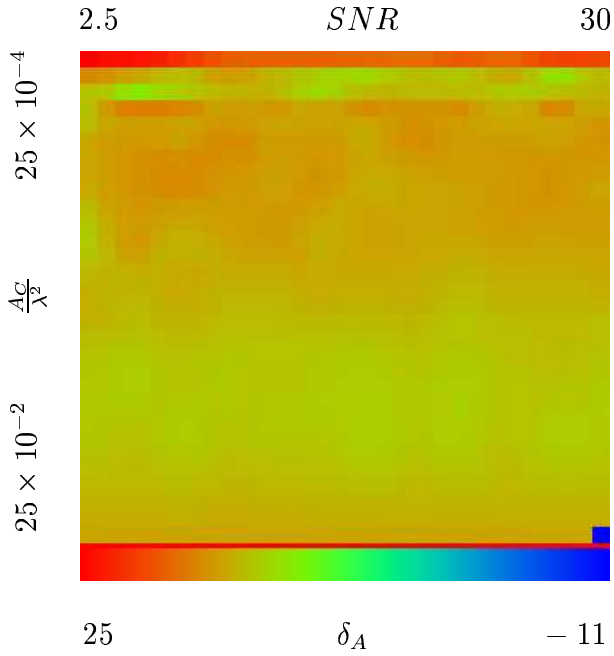

(d)

Fig. 3(*II*) - S. Caorsi et *al.*, "Improved Microwave Imaging Procedure ..."

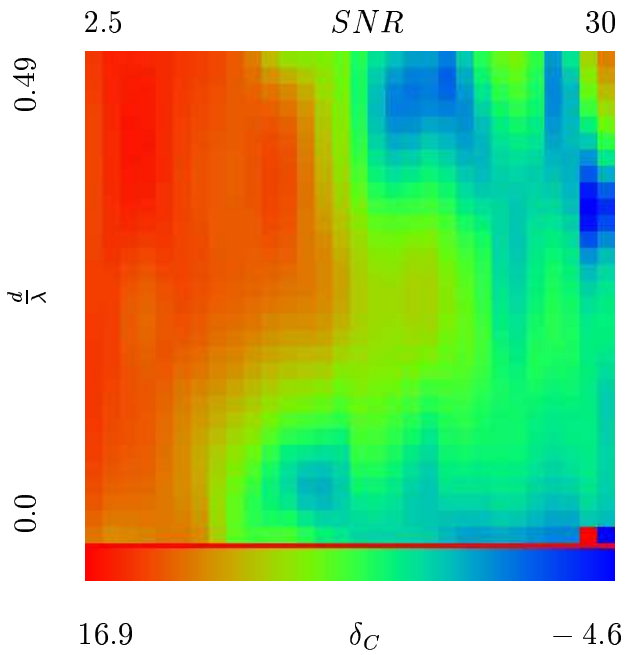

(a)

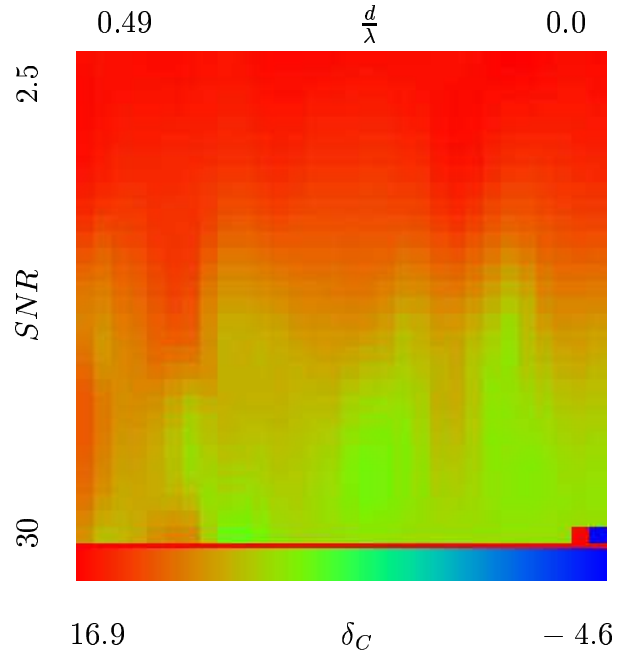

(b)

Fig. 4(I) - S. Caorsi et *al.*, "Improved Microwave Imaging Procedure ..."

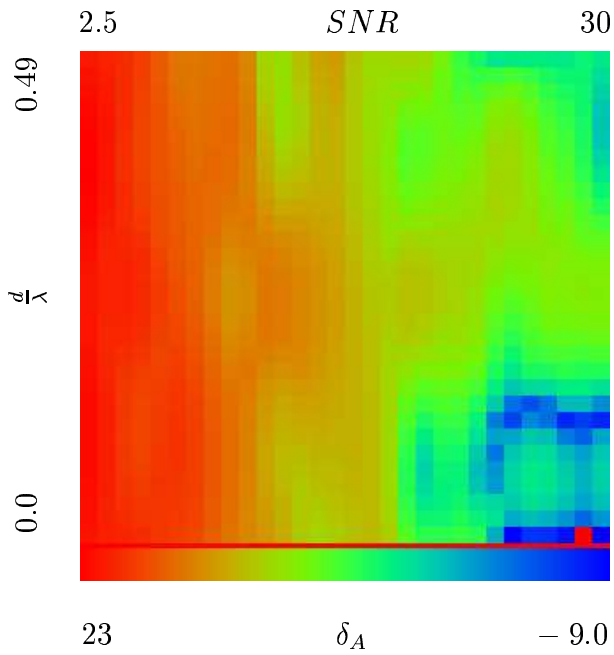

(a)

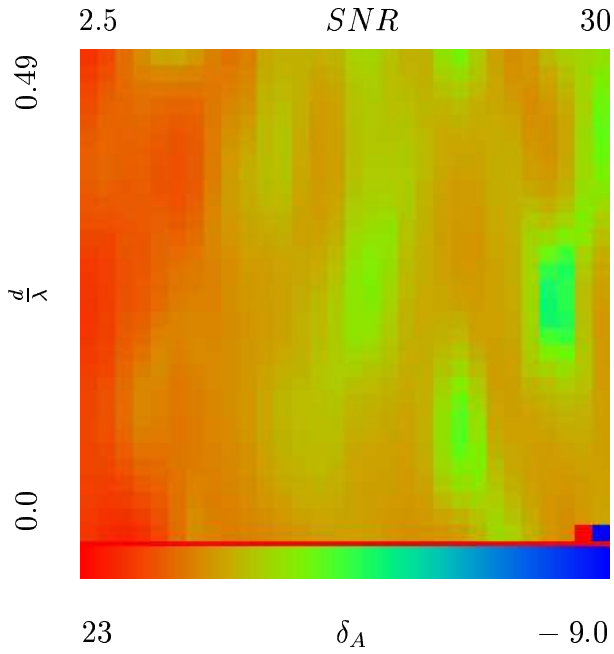

(b)

Fig. 4(*II*) - S. Caorsi et *al.*, "Improved Microwave Imaging Procedure ..."

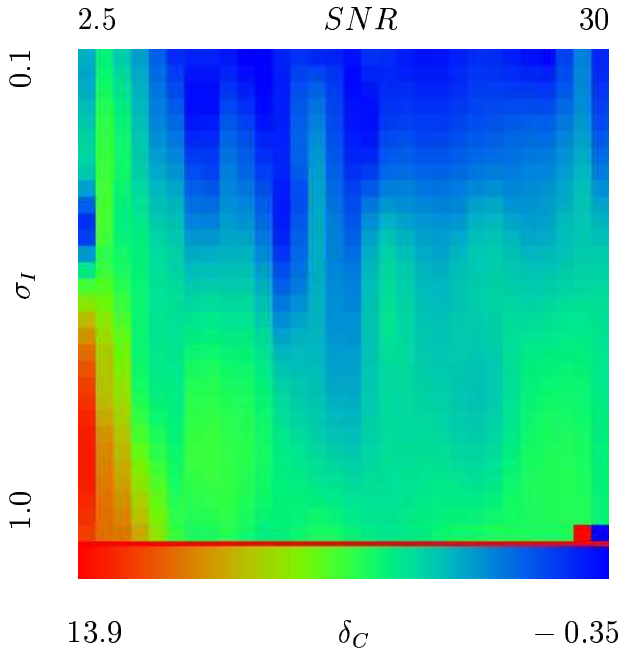

(a)

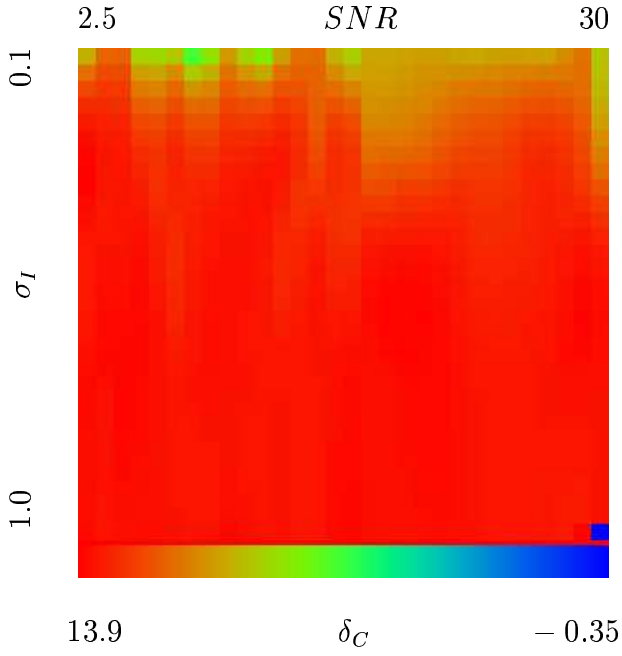

(b)

Fig. 5(I) - S. Caorsi et *al.*, "Improved Microwave Imaging Procedure ..."

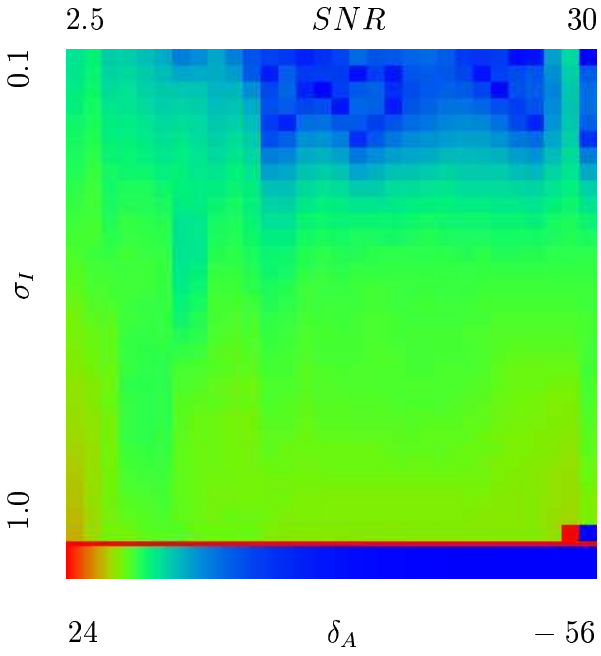

(c)

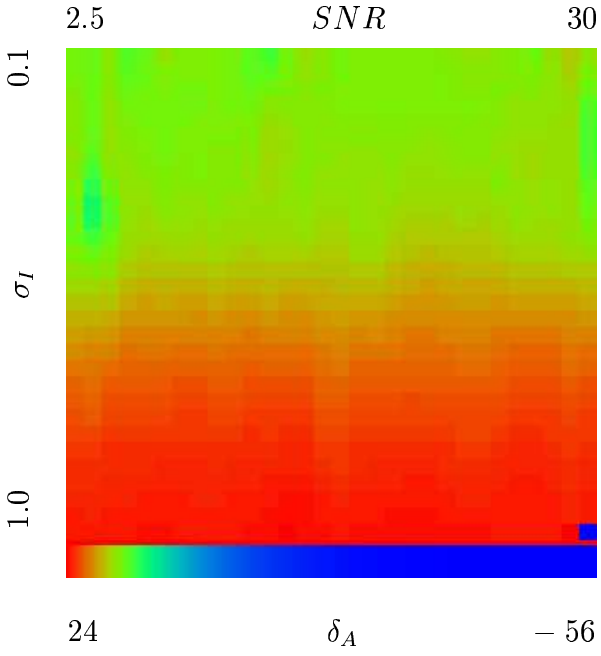

(d)

Fig. 5(*II*) - S. Caorsi et *al.*, "Improved Microwave Imaging Procedure ..."

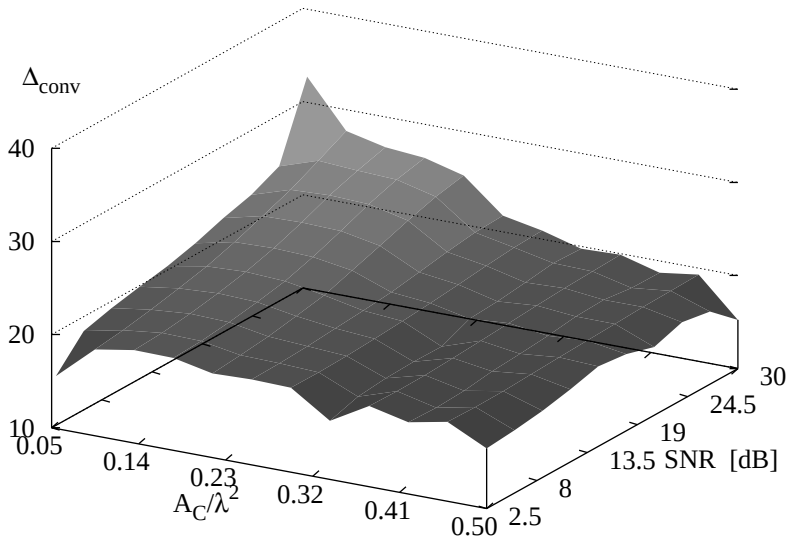

(a)

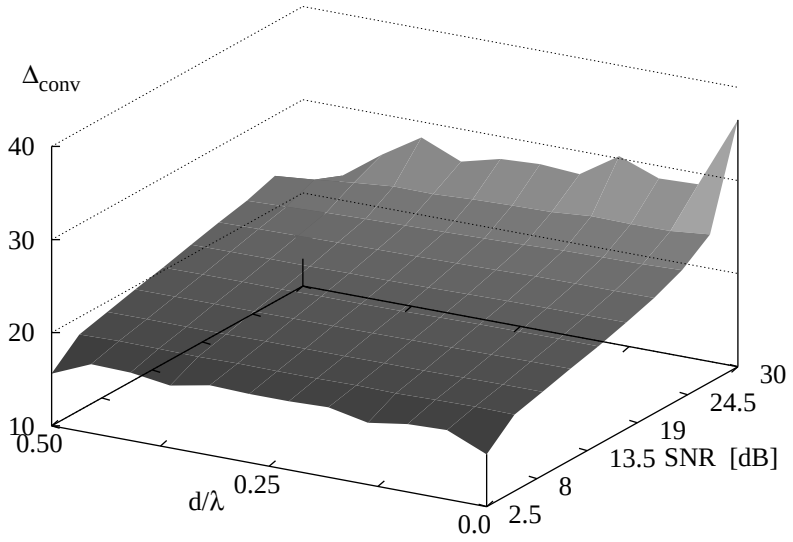

(b)

Fig. 6(I) - S. Caorsi et *al.*, "Improved Microwave Imaging Procedure ..."

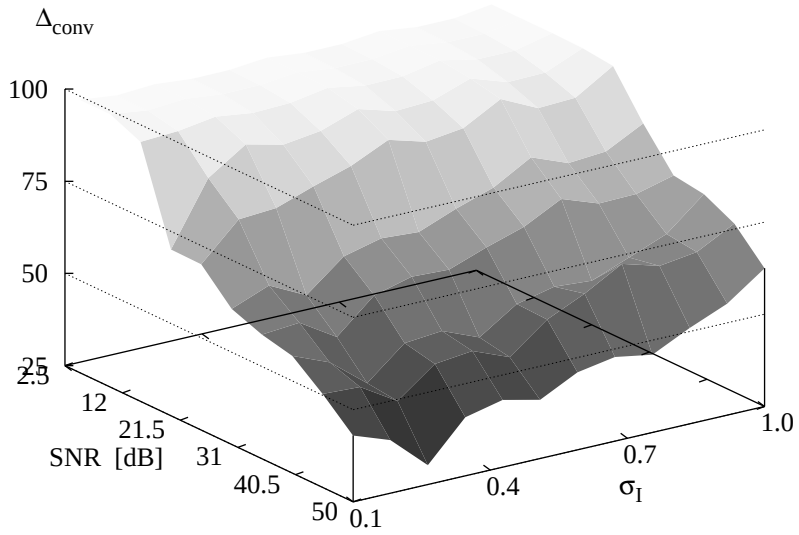

(c)

Fig. 6(*II*) - S. Caorsi et *al.*, "Improved Microwave Imaging Procedure ..."

	T_{min}	T_{max}	T_{av}
FGA	2.0	3.88	3.36
IGA	0.4	1.70	1.35

Tab. *I* - S. Caorsi et *al.*, "Improved Microwave Imaging Procedure ..."

	$Test\,Case\,1$	$Test\,Case\,2$	$Test\,Case\,3$
$av\left\{h^*_{FGA}\right\}$	329	322	439
$av\left\{h^*_{IGA}\right\}$	121	110	130
ξ^*	2.71	2.92	3.37

Tab. *II* - S. Caorsi et *al.*, "Improved Microwave Imaging Procedure ..."